Operational Calibration of the Meteosat Radiometer VIS Band

Yves M. Govaerts, Marco Clerici, and Nicolas Clerbaux

***Abstract*—An advanced operational algorithm has been developed for the routine calibration of the Meteosat radiometer solar channel. The calibration method relies on calculated radiances over bright desert sites whereas ocean targets are used for consistency checks. Calibration errors are estimated accounting for the uncertainties of both the sensor spectral response characterization and target property description. This algorithm has been used to systematically calibrate Meteosat-5 and -7 observations. Results show that it is possible to calibrate the visible band with an estimated accuracy of about 6% when the sensor response characterization is reliable and to monitor the sensor long-term drift. These results are confirmed by Clouds and the Earth's Radiant Energy System observations.**

***Index Terms*—Calibration, Meteosat.**

I. Introduction

THE METEOSAT satellite system was designed nearly 30 years ago, essentially for operational imagery purposes. The primary objective of this program is the acquisition of earth atmosphere images and their near real-time dissemination to the meteorological user's community. Nevertheless, the potential value of the Meteosat Visible and Infrared Imager (MVIRI) data for climate monitoring should not be underestimated. During the late 1970s and early 1980s, spaceborne observations of the earth were very scarce, essentially limited to geostationary meteorological observations and a few polar platforms. The extent of the Meteosat observations, acquired every 30 min in almost identical conditions during more than 20 years, represents a potentially valuable input to monitor or understand regional climate processes [1].

A prerequisite to such quantitative exploitation is to perform the radiometer calibration as accurately and precisely as possible. As no onboard calibration device exists for the solar channel (referred to as the visible (VIS) band), various vicarious approaches have been proposed in the past, but these attempts remain limited and isolated efforts. These approaches can essentially be divided into three categories: 1) instrument cross calibration (e.g., [2]–[4]); 2) airborne calibration campaign [5]; and 3) radiative transfer modeling (e.g., [6]–[8]). These latter studies showed that calculated radiances can be used to derive absolute calibration coefficients on a regular basis with an accuracy comparable to the one derived from airborne campaigns, but also to monitor the sensor long-term drift. So far, none of these methods has been used on an operational basis, although this has been proven to be feasible for the thermal channels [9], [10]. This situation has limited the quantitative exploitation of the VIS band observations and constrained users to develop their own calibration method prior to the derivation of any geophysical parameters (e.g., [7] and [11]). The complexity of consistent calibration coefficient estimation for the seven MVIRI instruments should not be underestimated. One of the major challenging problem concerns the lack of reliable characterization of the VIS band spectral response prior to that on the Meteosat-7 instrument [12], so that postlaunch corrections might be required as is the case for the Advanced Very High Resolution Radiometer instrument onboard the National Oceanic and Atmospheric Administration polar platform [13]. As demonstrated by [14], two spectrally different calibration targets could be used to verify the reliability of the MVIRI VIS band spectral response characterization and to evaluate whether postlaunch adjustments should be envisaged.

The objective of this paper is to present the operational calibration method developed at EUMETSAT in support of meteorological and climate applications. This novel method explicitly accounts for the radiometric noise, the sensor spectral response error, and simulation uncertainties (see Section II). The choice of this method is discussed in [15] and relies on radiative transfer modeling over bright deserts as the primary calibration target type. Open sea surface targets are used to verify the consistency and reliability of the results. This novel calibration method has been integrated in an operational facility to permit a systematic calibration of both archived and currently acquired Meteosat VIS band observations, including an automated *a priori* estimation of the calibration error (Section III). Results obtained for the calibration of Meteosat-5 and -7 demonstrate that it is possible to calibrate the VIS band with an estimated accuracy of about $\pm 6\%$, but this error increases as the uncertainty of the sensor spectral response characterization increases, as shown in Section IV. The proposed method also permits the precise monitoring of the long-term drift of the instrument. These results have been confirmed with an independent calibration exercise relying on Clouds and the Earth's Radiant Energy System (CERES) as reference (Section V). It is thus expected that this new calibration method will increase the value of the Meteosat First Generation (MFG) mission to support climate monitoring activities.

Manuscript received January 22, 2004; revised May 11, 2004. This work was supported by the Meteosat Second Generation (MSG) Programme and was carried out at EUMETSAT in the framework of the EUMETSAT new mandate on operational climate monitoring and in preparation of the MSG/SEVIRI calibration.

Y. M. Govaerts is with EUMETSAT, D-64295 Darmstadt, Germany (e-mail: govaerts@eumetsat.de).

M. Clerici is with Makalumedia, Darmstadt, Germany, and also with the Inland and Marine Waters Unit, Institute for Environment and Sustainability, Joint Research Centre of the European Commission, Ispra, Italy.

N. Clerbaux is with the Royal Meteorological Institute of Belgium, B-1180 Brussels, Belgium.

Digital Object Identifier 10.1109/TGRS.2004.831882

II. Statement of the Problem

Vicarious calibration requires an independent estimation of the radiance entering a detector, often referred to as the calibration reference. This reference radiance should be characterized at the entrance of the instrument to account for the full optical path used under normal acquisition mode. The radiance actually reaching the detectors, referred to as the effective or band-weighted radiance $\tilde{L}$, and which is converted into digital counts K, depends thus on both the spectral radiance $R(\lambda)$ impinging on a spaceborne instrument at the wavelength λ and the normalized spectral response (NSR) of the sensor $\xi(\lambda)$

$$\tilde{L} = \int_{\lambda} R(\lambda)\xi(\lambda)\, d\lambda. \tag{1}$$

The NSR $\xi(\lambda)$ is normalized so that its maximum value is equal to one. On MVIRI, since the sensor responds linearly to the incoming radiation $R(\lambda)$, the digitalized output signal K can be represented in a simple way with

$$K = \gamma \int_{\lambda} \xi(\lambda)R(\lambda)\, d\lambda + K_0 \tag{2}$$

where γ is the sensor gain and K_0 its offset, i.e., the zero intercept. Calibrating remote sensing data corresponds thus to finding the best estimate of c_f on the basis of the observed count K when pointing toward the calibration reference $\tilde{L}$

$$c_f = \frac{\int_{\lambda} R(\lambda)\xi(\lambda)\, d\lambda}{K - K_0} = \frac{\tilde{L}}{K - K_0} \tag{3}$$

where $c_f = 1/\gamma$ is the so-called calibration coefficient. The offset value K_0 is known from deep space observations (see Appendix A). Hence, as can be seen from (3), the uncertainty characterization of both $R(\lambda)$ and $\xi(\lambda)$ are critical for the generation of reliable calibration coefficients. In the case of simulated the estimation of the top-of-atmosphere (TOA) spectral radiances $R(\lambda)$ is subject to target property errors, whereas the estimation of the effective radiance is additionally affected by errors in the prelaunch measurement of the NSR $\xi(\lambda)$. A meaningful calibration method should thus explicitly account for uncertainties in the characterization of $\xi(\lambda)$, since this error might be large for the VIS band.

Let us first examine the error $\delta R(\lambda)$ of the simulated spectral radiance $R(\lambda)$. Spectral radiance impinging on a spaceborne instrument at wavelength λ is determined by a set of independent parameters $\{\chi_d\}$ that defines the observation conditions and a set of state variables $\{\chi_p\}$ describing the radiative properties of the observed targets, i.e., the atmosphere and the underlying surface. The independent parameters include the sun and viewing angles, the time of observation and finally the target location. Large uniform targets have been selected (see Appendix B) so that independent variable errors, principally determined by geolocation imprecision, could be neglected. The bulk effort concerning the target description consists thus in the characterization of the state variables $\{\chi_p\}$ of the radiative transfer model and the estimation of their respective errors ϵ_p. It is, therefore, necessary to identify a set of targets for which it is possible to define as accurately as possible the atmospheric and surface parameters $\{\chi_p\}$ during a period similar to the Meteosat archive duration. Since it is not possible to document surface radiative properties retrospectively, it is preferable to select stable and uniform targets, as can be found in arid desert areas. Error in the estimation of $R(\lambda)$ is expressed as a quadratic sum of the uncertainty contribution ϵ_p of each parameter χ_p

$$\delta R(\lambda) = \sqrt{\sum_{p=1}^{P} \left(\frac{\partial R(\lambda)}{\partial \chi_p}\right)^2 \epsilon_p^2} \tag{4}$$

where P is the number of parameters. The partial derivative of the outgoing radiance $\partial R(\lambda)/\partial \chi_p$ with respect to the parameter χ_p represents the sensitivity of the spectral radiance $R(\lambda)$ at wavelength λ for a specified set of independent parameters solely due to small perturbations in state variable χ_p [8]. An example of the estimation of $R(\lambda)$ and $\delta R(\lambda)$ over a desert and sea targets is shown in Fig. 1, top panel. Typical relative errors range between 10% to 15% within the VIS band spectral interval for one single simulation.

Let us now consider the error $\delta\xi(\lambda)$ of the NSR characterization $\xi(\lambda)$. Unfortunately, the shape of $\xi(\lambda)$ for the VIS band of MVIRI prior to Meteosat-7 has been poorly characterized. Only some scarce and unreliable measurements exist in the 0.5–0.9-μm interval. Values outside this interval are simply extrapolated. Since this error has not been characterized prior to the launch, a theoretical estimation is proposed in Appendix A that accounts for the errors on the wavelength definition accuracy, the instrument transmittance measurement and finally the extrapolation outside the characterization interval. An example of NSR error is shown in Fig. 1, bottom panel.

As can be seen in Fig. 1, spectral radiance over desert and sea notably differs, both in shape and intensity, but the ratio $\tilde{L}/K - K_0$ should be the same for these two cases when the NSR characterization is reliable and the radiometer responds linearly with respect to incoming radiation. Erroneous $\xi(\lambda)$ characterization might lead to inconsistent calibration results, i.e., that differ according to the spectral characteristics of the calibration reference. Sea and desert targets offer thus a possibility to control the reliability of the NSR characterization, provided the estimation of $R(\lambda)$ is accurate enough. Recent studies have demonstrated that simulations over desert targets have an average accuracy of about 3% when many observations are used [16]. Hence, desert targets are used as primary calibration targets whereas sea targets are used for consistency check purposes. The accuracy of calibration coefficients derived with simulated data is thus constrained by all the uncertainties associated with the input data as well as their propagation throughout the various calibration processing steps. A method to estimate and minimize these errors is described in the next section.

III. Operational Calibration Method

A. Overview

As seen in the previous section, the calibration coefficient estimation is affected both by calculated radiance uncertainties and the instrument characteristic errors. It is, therefore, necessary to estimate the corresponding impact on c_f accuracy and, if possible, to minimize this error. The processing of a large amount of data should permit the reduction of the calibration errors, provided that these errors are independent and random, i.e., not systematic. The proposed calibration algorithm is designed to minimize the error propagation while deriving a calibration coefficient. A twofold strategy has been developed to reduce the error. First, a target identification process takes place to find cases

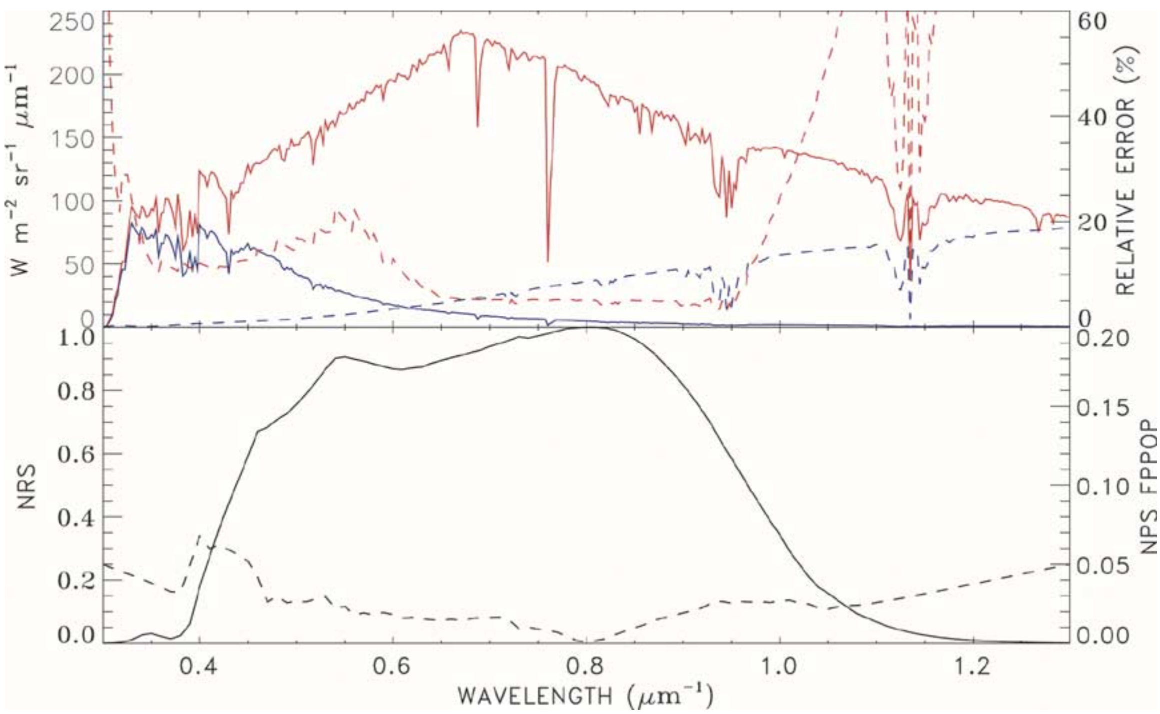

Fig. 1. (Top) Typical simulated TOA spectral radiance over a desert target (solid red line) and sea (solid blue line). Estimated errors are shown with dashed lines. (Bottom) NSR of (solid line) the MVIRI VIS band onboard Meteosat-7 and (dashed line) the estimated absolute characterization error.

where the target parameter error ϵ_p is minimum. For instance, calibration over sea target will not take place when surface wind speed exceeds 7 ms^{-1}, i.e., when foam starts to appear at the sea surface. Under these conditions, the simulated radiance will be highly sensitive to any error in the wind speed estimation. To increase the probability of finding such ideal situations, the calibration relies on the acquisition of data during an accumulation period $[p_1, p_2]$ ranging typically from five to ten days. Second, an error reduction based on temporal and spatial averaging of the results is applied to detect inconsistent results, if any, and to reduce the effects due to random errors. All errors are estimated for a given interval of confidence α, usually set to 95%.

Whenever possible throughout this error reduction technique, it is necessary to discriminate systematic from random errors. Atmospheric parameter errors are essentially controlled by the aerosol load uncertainty. Since this amount is derived from a climate dataset [16], temporal errors might be systematic during a calibration period. It is, however, assumed that these errors are not spatially correlated as the aerosol amount can change rapidly from place to place, particularly over desert areas. Similarly, since desert target properties are very stable, any uncertainty in the characterization of these properties will be responsible for systematic errors in time. It is actually expected that the simple bare soil bidirectional reflectance (BRF) model [17] used in this study fails to represent accurately specific anisotropy effects resulting from sand dune spatial organization. It is, however, assumed that errors in the characterization of target surface properties are not correlated in space, as these sand dune linear arrangements differ from target to target. This assumption is debatable, but is applied for error handling convenience. Actually, a recent study has revealed a systematic bias of about 3% between simulated radiances and calibrated Along-Track Scanning Radiometer (ATSR-2), Sea-viewing Wide Field-of-view Sensor (SeaWiFS), VEGETATION, and Medium Resolution Imaging Spectrometer (MERIS) observations acquired over these targets [16]. This bias is within the range of these instrument calibration accuracies and is, thus, currently not explicitly taken into account in the error estimation scheme.

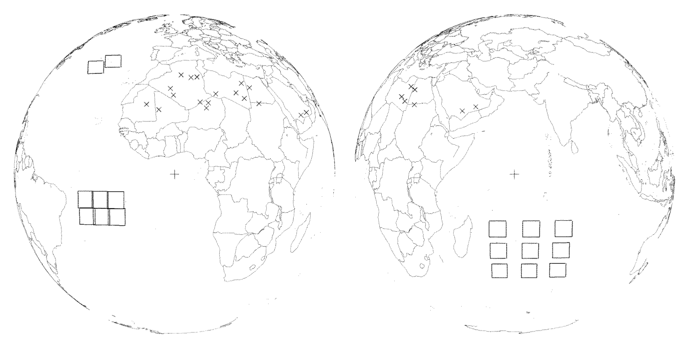

Fig. 2. Location of the calibration targets for the (left) 0° nominal subsatellite position, shown with the + symbol, and (right) 63° east one. Desert target locations are indicated with the × symbol and sea search areas with square boxes.

B. Target Identification

For each analyzed image during a calibration period $[p_1, p_2]$, an identification process takes place to select potential targets whose actual properties and observation/illumination angles correspond to cases where calculated radiance error is minimum. Over desert targets (Fig. 2), cloud and sand storm cases are identified by analyzing daily variation of the observed count values. Clear-sky pixel detection is performed by fitting a second order polynomial to the daily cycle of observations (Fig. 3). Any deviation from this polynomial is interpreted as a cloud contamination, cloud shadow, or sand storm. Observations of that day are disregarded when the remaining number of clear-sky slots is too low after this daily filtering. Sea targets are defined by large search

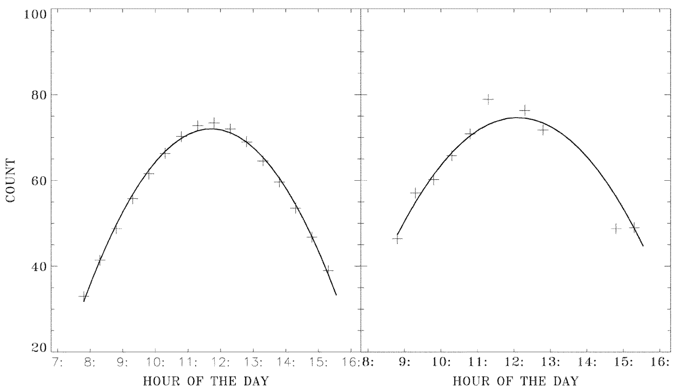

Fig. 3. (Left) Digital count daily variations (+ symbol) over a desert target exhibit regular changes that can be fitted with a parabola (solid line) during clear-sky days. These observations have been acquired by Meteosat-7 on November the first of 1998 over target Algeria 1 [18]. (Right) Clouds (cloud shadow or sand storms) show positive (negative) deviation from the fitted parabola. These observations have been acquired by Meteosat-7 on November 4, 1998, over target Algeria 1 [18].

areas, shown in Fig. 2, in which cloud- and aerosol-free potential targets are identified, looking at uniform and very low digital count values outside the sun-glint regions. This procedure is used to ensure a very low aerosol optical thickness. The values of the surface wind speed and the total column water vapor are extracted from European Centre for Medium-Range Weather Forecasts (ECMWF) data, and a potential target is disregarded when the wind speed exceeds 7 ms^{-1}.

When a target g is successfully identified within an image acquired at time t, the $N_c \times N_l$ pixels centered on the target location are extracted from the corresponding image. The average value $\hat{K}(g,t)$, minimum $K_{\min}(g,t)$, maximum $K_{\max}(g,t)$, and error $\delta\hat{K}(g,t)$ of the observed pixel count values over that site g are next evaluated. The associated radiometric error is estimated at confidence level α accounting for both the instrument noise $\delta K_{1.5}(t)$ and any deviation from the target uniformity

$$\delta\hat{K}(g,t) = \frac{t_{\alpha/2}(N_l N_c - 1)}{\sqrt{N_l N_c}} \cdot \sqrt{(\delta K_{1.5}(t))^2 + \frac{1}{N_l N_c - 1}\sum_{i,j}^{N_l N_c}(K(i,j,t) - \hat{K}(g,t))^2} \quad (5)$$

where $K(i,j,t)$ is the digital count of pixel (i,j) at time t within the target g area, and $t_{\alpha/2}(N_l N_c - 1)$ is the Student's percentiles at confidence level α for $N_l N_c - 1$ degrees of freedom. The estimation of $\delta K_{1.5}(t)$ is given in Appendix A. Since targets are very uniform areas, the values $|K_{\max}(g,t) - K_{\min}(g,t)|$ and $\delta\hat{K}(g,t)/\hat{K}(g,t)$ are expected to be small. An observation is rejected when it is not the case.

C. Radiative Transfer Modeling

Spectral radiances are calculated with the 6S code [19] for all successfully identified targets accounting for the actual illumination and viewing angles at the acquisition time t and the surface and atmospheric properties $\chi_p = \{\chi_s, \chi_a\}$. TOA spectral radiance errors are due to individual state variable error ϵ_p [see (4)] and radiative transfer model (RTM) error $\delta R_m(\lambda)$, i.e., imprecision of the calculation procedure not related to errors in the model input parameters [6]. According to RTM comparisons over anisotropic surfaces [20], this error is estimated for the 6S code as a simple function of the sun zenith angle (SZA) θ_s

$$\delta R_m(\lambda) = R(\lambda)\left(\epsilon_{M1} + \epsilon_{M2}\left(\frac{\theta_s}{\pi}\right)^2\right) \quad (6)$$

where ϵ_{M1} and ϵ_{M2} are set to 0.025 and 0.060. Assuming that the surface, atmospheric, and model errors are independent, the outgoing TOA spectral radiance error at a particular wavelength $\delta R(\lambda)$ can be written as the quadratic sum of all these contributions

$$\delta R(\lambda) = \sqrt{(\delta R_m(\lambda))^2 + (\delta R_a(\lambda))^2 + (\delta R_s(\lambda))^2} \quad (7)$$

where $\delta R_a(\lambda)$ and $\delta R_s(\lambda)$ are the spectral radiance errors from the atmosphere and the surface, respectively. Solar irradiance $I(\lambda)$ error is not included in (7), since the calibration coefficient is calculated for a given effective irradiance value $\tilde{I}(\lambda) = \int_\lambda \xi(\lambda)I(\lambda)\,d\lambda$ that can subsequently be used to convert observed radiances into bidirectional reflectance factors.

The effective radiance $\tilde{L}(g,t)$ over target g at time t, evaluated with (1), is affected both by $\delta R(\lambda)$ and $\delta\xi(\lambda)$. The estimation of the corresponding effective radiance error is calculated assuming that: 1) the error $\delta\xi(\lambda)$ is systematic and not correlated with $\delta R(\lambda)$ and 2) the errors $\delta\xi(\lambda)$ and $\delta R(\lambda)$ are function of the wavelength. Under these assumptions and those of (7), the estimated effective radiance error can be written as the quadratic sum of the uncertainty contributions due to the RTM, the atmosphere and surface characterization, and finally the instrument spectral response, as in (8), shown at the bottom of the page, where

$$\delta\tilde{L}_m(g,t) = \int_\lambda \xi(\lambda)\delta R_m(\lambda,g,t)\,d\lambda$$
$$\delta\tilde{L}_a(g,t) = \int_\lambda \xi(\lambda)\delta R_a(\lambda,g,t)\,d\lambda$$
$$\delta\tilde{L}_s(g,t) = \int_\lambda \xi(\lambda)\delta R_s(\lambda,g,t)\,d\lambda$$
$$\delta\tilde{L}_\xi(g,t) = \int_\lambda \delta\xi(\lambda)R(\lambda,g,t)\,d\lambda.$$

D. Calibration

1) Calibration of Individual Observations: The time series composed of pairs of observed count and simulated radiance are accumulated individually for each target g during the period $[p_1, p_2]$. A calibration coefficient $c_f(t,g)$ is estimated for each pair of the time series with (3). The corresponding error is

$$\delta\tilde{L}(g,t) = \sqrt{(\delta\tilde{L}_m(g,t))^2 + (\delta\tilde{L}_a(g,t))^2 + (\delta\tilde{L}_s(g,t))^2 + (\delta\tilde{L}_\xi(g,t))^2} \quad (8)$$

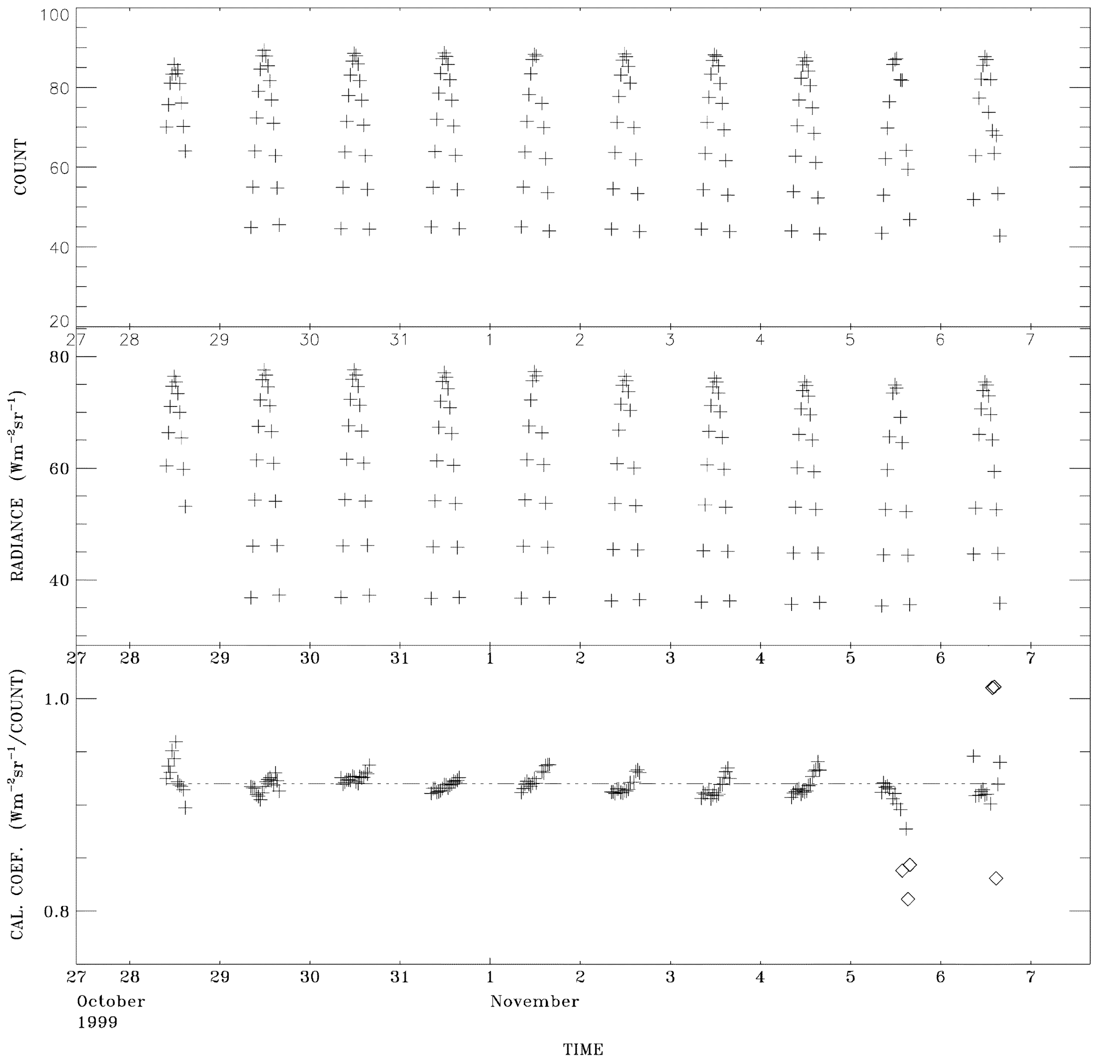

Fig. 4. Example of a ten-day time series over target Mali 1 [18]. (Top) Successfully identified clear-sky counts (+ symbol) observed by Meteosat-7. (Middle) Simulated TOA radiances. (Bottom) Estimated calibration coefficients (+ symbol). Coefficients which are significantly different at the 95% level from the mean value (horizontal dash-dotted line) are shown with the ⋄ symbol.

expressed as the quadratic sum of the radiance and radiometric relative errors as in (9), shown at the bottom of the page, where

$$\delta_r\tilde{L}_m = \frac{\delta\tilde{L}_m(t,g)}{\tilde{L}(t,g)}$$
$$\delta_r\tilde{L}_s = \frac{\delta\tilde{L}_s(t,g)}{\tilde{L}(t,g)}$$
$$\delta_r\tilde{L}_a = \frac{\delta\tilde{L}_a(t,g)}{\tilde{L}(t,g)}$$
$$\delta_r\tilde{L}_\xi = \frac{\delta\tilde{L}_\xi(t,g)}{\tilde{L}(t,g)}$$
$$\delta_r\hat{K} = \frac{\delta\hat{K}(t,g)}{\hat{K}(t,g)-K_0(t)}$$
$$\delta_r\hat{K}_0 = \frac{\delta\hat{K}_0(t)}{\hat{K}(t,g)-K_0(t)}$$

and $\delta\hat{K}_0(t)$ is the standard deviation of $\hat{K}_0(t)$ estimated over each space corner (see Appendix A).

2) Temporal Averaging: Fig. 4 shows an example of a ten-day calibration time series over one desert target. As can be seen, the coefficients $c_f(t,g)$ take some extreme values most likely due to undetected atmospheric perturbation like broken cloud fields. Such coefficients are disregarded when there are statistically different from the mean value. A temporal averaging of the N_g remaining coefficients $c_f(t,g)$ derived over each target g is performed to reduce random error effects due to the radiometric noises $\delta_r\hat{K}$ and $\delta_r\hat{K}_0$. The weighted mean calibration coefficient $\bar{c}_f(g)$ over a target g during period $[p_1,p_2]$ is estimated using normalized weights $\kappa_f(t,g)$ inversely proportional to the calibration coefficient error

$$\kappa_f(t,g) = \left(\frac{1}{\delta c_f(t,g)}\right)^2 \Bigg/ \sum_{t\in[p_1,p_2]} \left(\frac{1}{\delta c_f(t,g)}\right)^2. \quad (10)$$

$$\delta c_f(t,g) = c_f(t,g)\sqrt{(\delta_r\tilde{L}_m)^2+(\delta_r\tilde{L}_a)^2+(\delta_r\tilde{L}_s)^2+(\delta_r\tilde{L}_\xi)^2+(\delta_r\hat{K})^2+(\delta_r\hat{K}_0)^2} \quad (9)$$

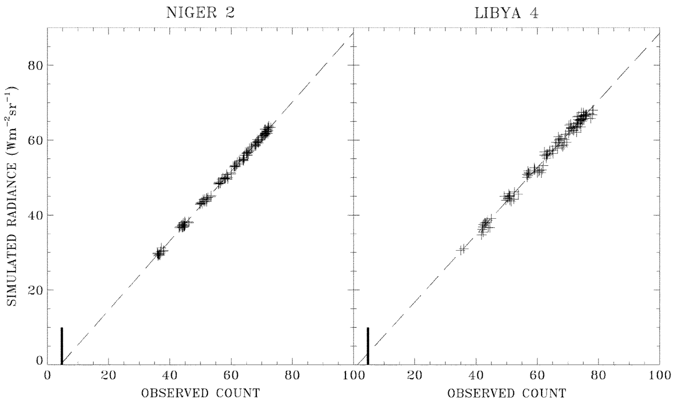

Fig. 5. Example of the daily fit consistency check based on the retrieval of the space count value during a ten-day calibration period running from October 28 to November 16, 999. During that calibration period, the mean offset value $\hat{\hat{K}}_0$ is equal to 4.82 ± 0.40 (thick vertical bar). The linear regression is shown with the dashed line. The left panel illustrates a successfully retrieved offset value whereas the right panel illustrates a case of failure.

Assuming that radiometric errors are not correlated in time, the error $\delta\bar{c}_f(g)$ of the mean coefficient $\bar{c}_f(g)$ is written as in (11), shown at the bottom of the page, where $\sigma_{\bar{c}_f}(g)$ is the weighted standard deviation of $\bar{c}_f(g)$. In this equation, the first four terms of the right side correspond to systematic errors and $t_{\alpha/2}(N_g-1)\sigma_{\bar{c}_f}(g)/\sqrt{N_g}$ is an estimation of the random error contribution at confidence α. Finally, targets with an estimated error $\delta\bar{c}_f(g)$ exceeding a threshold value are disregarded and will not be further processed.

An additional test is performed to verify the consistency of the mean coefficients $\bar{c}_f(g)$ derived over each desert target. Calculated radiance daily variations are compared with observations as suggested by [21]. When simulated daily variation is consistent with the observed one, it should be possible to retrieve the offset value as explained in Appendix C. This retrieved offset value K_0' is compared with the mean actual one, $\hat{\hat{K}}_0$, derived from deep space observations. In case the surface BRF or the aerosol load is not correct, simulated radiances will exhibit a systematic bias with respect to the observed count value as illustrated in Fig. 5. A target is disregarded when the derived space count value K_0' is significantly different at confidence level α from the actual one $\hat{\hat{K}}_0$ (right panel). Conversely, when simulations are reliable, K_0' and $\hat{\hat{K}}_0$ are similar (left panel) and the target is kept for further processing.

3) Spatial Averaging: So far, a temporal mean calibration coefficient has been derived separately over each desert target g as can be seen on Fig. 6. All successfully derived coefficients $\bar{c}_f(g)$ are now spatially averaged, assuming that the atmosphere and surface characterization errors are not correlated in space. Since spectral properties of desert targets (referred to as type D) are quite similar, these coefficients should normally be very close, even in case of large errors in the characterization of the sensor response. Hence, outliers, if any, are expected to result from modeling errors and are disregarded.

The weighted mean calibration coefficient $\hat{\bar{c}}_f(D)$ over the N_D desert targets is equal to

$$\hat{\bar{c}}_f(D) = \sum_{g=1}^{N_D} \bar{\kappa}_f(g)\bar{c}_f(g) \tag{12}$$

where $\bar{\kappa}_f(g)$ is the weight of each target with

$$\bar{\kappa}_f(g) = \left(\frac{1}{\delta\bar{c}_f(g)}\right)^2 \Bigg/ \sum_{g=1}^{N_D}\left(\frac{1}{\delta\bar{c}_f(g)}\right)^2. \tag{13}$$

The error of $\bar{c}_f(D)$ is estimated assuming that the state variable error is not spatially correlated as previously discussed, as in (14), shown at the bottom of the page. These error contributions are illustrated on Fig. 6. The coefficient $\bar{c}_f(D)$ derived over the desert targets and its associated error $\delta\hat{\bar{c}}_f(D)$ represent the two major outputs of the operational calibration algorithm when it is applied over a period $[p_1, p_2]$.

4) Final Consistency Check: An ultimate test is performed to verify the reliability of $\hat{\bar{c}}_f(D)$ and $\delta\hat{\bar{c}}_f(D)$. To this end, a calibration coefficient is derived over sea $\hat{\bar{c}}_f(S)$ in a similar way, except for the daily cycle analysis presented in Appendix C which is not applied in this case, the amplitude of the daily variation being too small with respect to simulation errors. As stated in Section II, calibration coefficients derived over desert and sea targets should be similar if: 1) the radiometer responds linearly to the incoming radiance intensity; 2) the characterization of the sensor spectral response is correct; and finally 3) the radiative transfer simulations are reliable. When these conditions are met, the difference between the calibration coefficients derived over each target type should be smaller than the corresponding error. This condition can be translated into the following probability

$$\delta\bar{c}_f(g) = \sqrt{\frac{\bar{c}_f^2(g)}{N_g}\sum_{t\in[p_1,p_2]}\left((\delta_r\tilde{L}_m)^2 + (\delta_r\tilde{L}_a)^2 + (\delta_r\tilde{L}_s)^2 + (\delta_r\tilde{L}_\xi)^2\right) + \frac{t_{\alpha/2}^2(N_g-1)}{N_g}\sigma_{\bar{c}_f}^2(g)} \tag{11}$$

$$\delta\hat{\bar{c}}_f(D) = \sqrt{\frac{\hat{\bar{c}}_f^2(D)}{N_D}\sum_{g\in D}\left((\delta_r\tilde{L}_m)^2 + (\delta_r\tilde{L}_\xi)^2\right) + \frac{t_{\alpha/2}^2(N_D-1)}{N_D}\sigma_{\hat{\bar{c}}_f}^2(D)} \tag{14}$$

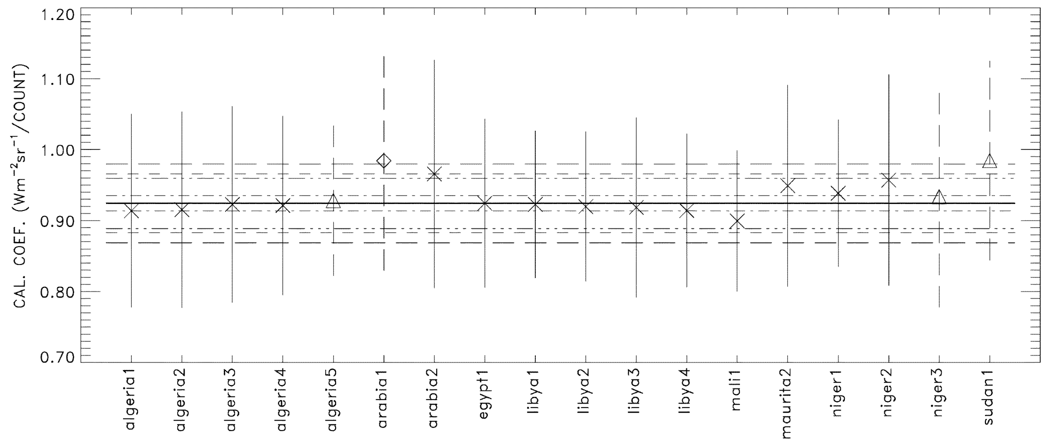

Fig. 6. Example of the mean calibration coefficient $\bar{c}_f(g)$ distribution derived over each desert target ($\times$ symbol) for a period running from 20 October to 6 November 1998. The associated error is represented with a vertical solid line. Targets with a $\bar{c}_f(g)$ value significantly different from the mean value are shown with a $\diamond$ symbol and with an erroneous retrieved space count value with a $\triangle$ symbol. The horizontal lines have the following meaning: — (solid) line represents the weighted mean value $\hat{\bar{c}}_f(D)$; – – (long dashes) lines correspond to the total error at the 95% confidence level $\delta\hat{\bar{c}}_f(D)$; - - - (dashes) line is for the RTM model error contribution; the —$\cdots$ (dash-do-dot-dot) lines are for the NSR error contribution and -$\cdot$ (dash dot) lines are for the random error contribution.

$P\{\hat{\bar{c}}_f(D) = \hat{\bar{c}}_f(S)\}$ which is approximated by a Student's distribution

$$t_s = \frac{|\hat{\bar{c}}_f(D) - \hat{\bar{c}}_f(S)|}{\sqrt{\sigma^2_{\hat{\bar{c}}_f}(D) + \sigma^2_{\hat{\bar{c}}_f}(S)}} \tag{15}$$

with a number of degrees of freedom equal to

$$\nu = \frac{\left(\sigma^2_{\hat{\bar{c}}_f}(D) + \sigma^2_{\hat{\bar{c}}_f}(S)\right)^2}{\frac{\sigma^4_{\hat{\bar{c}}_f}(D)}{N_D - 1} + \frac{\sigma^4_{\hat{\bar{c}}_f}(S)}{N_S - 1}}. \tag{16}$$

The coefficients derived over desert and sea targets might be very close but still be affected by a similar bias. An additional test is, therefore, applied to verify the consistency of the results, based on a similar reasoning as in (23) to retrieve the space count. This test is performed accounting for all the observations over both sea and desert targets that have successfully passed all the previous consistency checks. The probability $P\{K_0 = K_0'\}$ is calculated similarly as $P\{\hat{\bar{c}}_f(D) = \hat{\bar{c}}_f(S)\}$. The mean value of these two probabilities is used as a single quality indicator P_c. When P_c is lower than $1 - \alpha$, the calibration result is disregarded. Different scenarios should be considered. A situation where P_c would always be taking low values indicates a problem probably due to the characterization of the instrument spectral response. Such situation requires an update of the prelaunch NSR characterization, as already done for the Meteosat-5 and -6 instruments [14]. When only a limited number of processed periods present suspicious results, this could be due to specific meteorological conditions which are not correctly represented in the climatic datasets used for the calibration. These periods are not taken into account for the monitoring of the sensor long-term drift.

E. Sensor Drift

The long-term drift of the MVIRI VIS band is estimated assuming a linear degradation of the sensor sensitivity

$$\breve{c}_f(t) = \breve{c}_f(t_0) + \mathcal{D}_f n_t \tag{17}$$

where $\breve{c}_f(t_0)$ is the estimated calibration coefficient at launch time $t_0, \mathcal{D}_f$ is the daily degradation rate and n_t the number of days since launch. The values of $\breve{c}_f(t_0)$ and $\mathcal{D}_f$ are derived from a linear regression performed on all available $\hat{\bar{c}}_f$. The corresponding error $\delta\breve{c}_f(t_0)$ and $\delta\mathcal{D}_f$ are estimated at the confidence level α in a similar way as in (24) and (25). From these equations, the error of $\breve{c}_f(t)$ could be estimated for any date t as

$$\delta\breve{c}_f(t) = \sqrt{(\delta\breve{c}_f(t_0))^2 + (n_t \delta\mathcal{D}_f)^2}. \tag{18}$$

IV. Results

The algorithm has been applied for the calibration of the MVIRI VIS band onboard Meteosat-5 and -7 launched, respectively, on 2 March 1991 and 2 September 1997. Since July 1998, Meteosat-5 has been operated at 63° E, originally in support to the Indian Ocean Experiment (INDOEX). Except when data were not available, the algorithm has been applied four times a year during ten-day periods ranging from Julian days 31–40, 121–130, 211–220, and 301–310. The calibration was performed using Meteosat images extracted from the EUMETSAT archive in native rectified format (RECT2LP). Results are shown in Figs. 7 and 8 for the MVIRI VIS band onboard Meteosat-7 and -5, respectively.

The efficiency of the calibration error reduction technique, i.e., the decrease in error from the estimation of the calibration coefficient based on a single count/simulated radiance pair (9) up to the spatial averaging (14) is examined first. For that purpose, the mean relative errors $\delta_r c_f(t,g)$, $\delta_r \bar{c}_f(g)$, and $\delta_r \hat{\bar{c}}_f$ were estimated using all valid observations of each processed period. The contribution of each error term was estimated in a similar way. Results are shown in Tables I–III. Over desert targets, the error δc_f is largely dominated by surface characterization uncertainty for Meteosat-7 whereas surface, and NSR uncertainties have a similar impact for Meteosat-5. Temporal averaging has almost no effect on the total calibration error $\delta_r \bar{c}_f$ as a result of the small contribution of the radiometric relative errors, about 1%, compared to the other terms. Conversely, space averaging significantly decreases the total error as it essentially acts on the

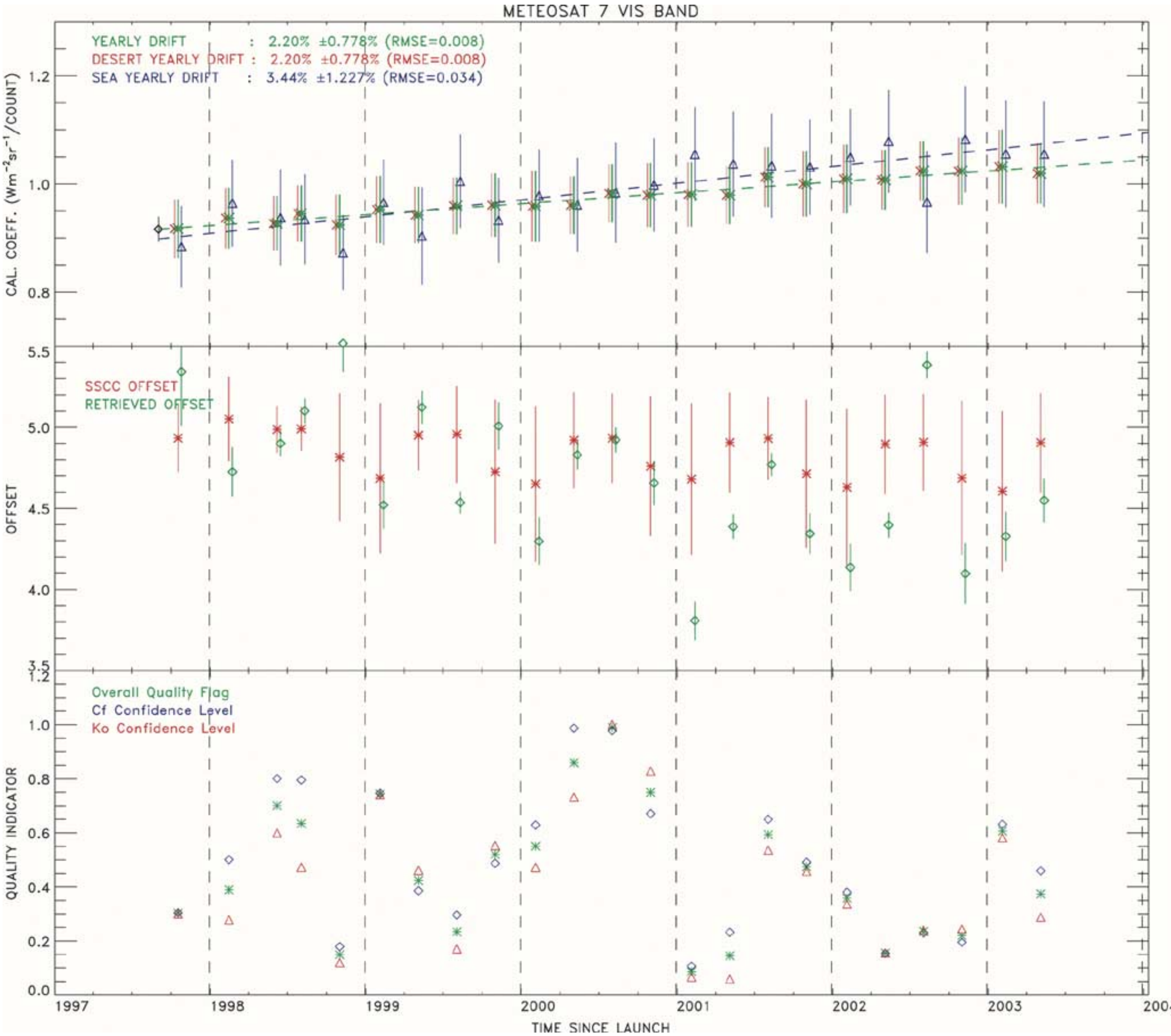

Fig. 7. (Top) Meteosat-7 VIS band calibration coefficients $\hat{c}_f(p)$ derived during each application cycle of SSCC over desert target (× red symbols) and sea (△ blue symbols). The estimated error $\delta\hat{c}_f(p)$ is shown with the vertical bars. The red (blue) dashed line indicates the estimated linear sensor drift over desert and sea targets. The black ⋄ symbol is for the calibration coefficients estimated at the launch time, with the associated error shown with the black vertical bars. (Middle) Mean offset value in digital count (∗ red symbols) and associated error (red vertical bars). The retrieved offset value is shown with the green ⋄ symbol. (Bottom) The probability $P\{\hat{c}_f(D) = \hat{c}_f(S)\}$ is shown with the blue ⋄ symbol, the probability $P\{K_0 = K_0'\}$ with the red △ symbol, and the overall quality indicator is shown with the ∗ green symbol.

surface and atmosphere state variable error. The residual random error is close to 1.5%, and the total error is now dominated by RTM and NSR uncertainties. For each processed ten-day period, calibration coefficients $\hat{c}_f(p)$ are derived with an estimated error of about 6% for Meteosat-7. The Meteosat-5 displacement from 0° to 63° had no significant impact on the calibration accuracy despite only seven desert targets being visible from the 63°E position. The very high contribution of the NSR uncertainty to the total error explains this result.

Error propagation is somewhat different over sea targets. No surface errors are considered, since surface conditions are only determined by the wind speed and direction (see Appendix B) that translate into an error due to atmospheric condition uncertainty. This uncertainty dominates the single observation error but is similar in magnitude to the contribution of the NSR uncertainty for Meteosat-7. As a result, the total error after the temporal averaging is principally controlled by this latter contribution. Sea surfaces being very uniform, whatever the search area, the spatial averaging minimally reduce the total error.

For Meteosat-7, the calibration coefficient derived at launch date (September 2, 1997) is equal to 0.916 ± 0.0233 $\mathrm{Wm^{-2}sr^{-1}}$/DC (2.5% relative error) with a daily drift equal to $5.523^{-5} \pm 1.953^{-5} \cdot \mathrm{Wm^{-2}sr^{-1}}$/DC/Day (see Table IV). There is very good agreement between the coefficients $\hat{c}_f$ derived with (12) and those resulting from the linear regression (Fig. 7, top panel). For instance, calibration coefficient $\hat{c}_f$ for period 31–40 of 2003 is 1.042 ± 0.0565 $\mathrm{Wm^{-2}sr^{-1}}$/DC, whereas $\check{c}_f$ estimated for the same period with (18) is equal to

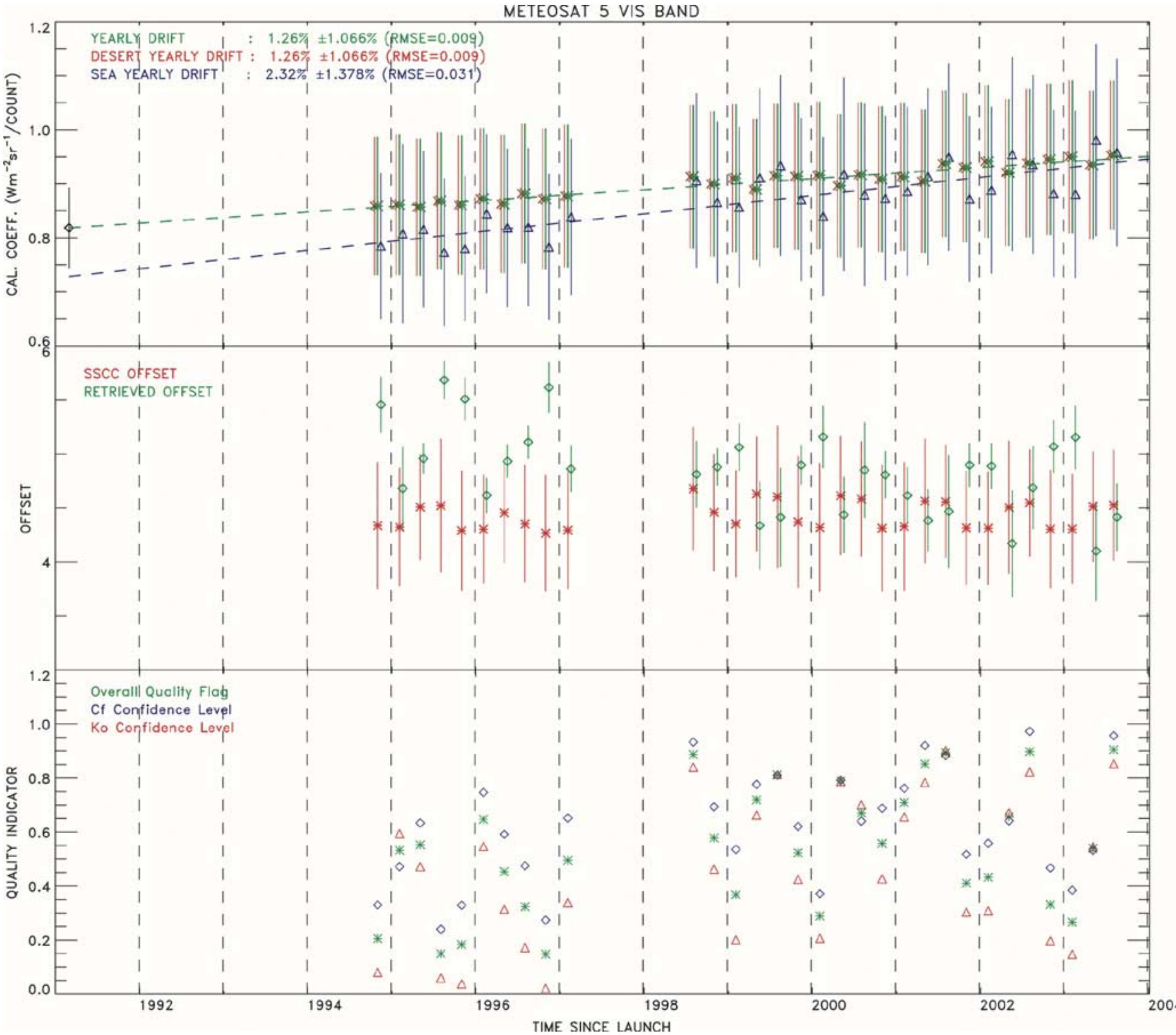

Fig. 8. Same as Fig. 7 but for Meteosat-5.

1.036 ± 0.0482. The yearly degradation rate is about 2.2% for Meteosat-7, showing a regular drift from calibration period to calibration period. Results over sea targets exhibit an important temporal variability, most likely due to the high sensitivity to aerosol conditions. Search areas located in the South Atlantic might be affected by biomass burning aerosols originating from southern Africa that are subject to large interannual variability.

For both sensors, the estimated drift over sea targets is much larger than the one derived over desert targets. Instrument optics and detector contamination, responsible for the observed drift, might be of different magnitude according to the wavelength. Often, short wavelengths are more sensitive to degradation. Such spectral behavior might explain the high drift observed over ocean, as spectral radiance over sea surface takes its maximum value around 0.4 μm, whereas maximum value occurs around 0.7 μm over desert surfaces (see Fig. 1).

The mean observed space count for Meteosat-7 is subject to regular seasonal variations (Fig. 7, medium panel) that might be related to changing instrument temperature. A detailed analysis, not shown here, reveals that one of the two VIS detectors is very stable in time with a mean value very close to five counts, whereas the offset of the second one oscillates between 4.5 and 5 counts. The retrieved offset values and the probabilities $P\{K_0 = K'_0\}$ also exhibit these variations, in particular during 2000 and 2001.

V. Evaluation

Several independent approaches have been used to evaluate the reliability of the calibration coefficient and its error. The calibration reference accuracy is evaluated first, comparing simulated radiances with calibrated observations acquired by

TABLE I
RELATIVE ERROR (PERCENT) CONTRIBUTION ON THE ESTIMATION OF THE CALIBRATION COEFFICIENT OF THE METEOSAT-7 RADIOMETER VIS BAND LOCATED AT 0°. THE RADIOMETRIC ERROR δK_T IS EQUAL $\sqrt{\delta\hat{K}^2 + \delta\hat{K}_0^2}/\hat{K}$. RAND IS THE MEAN RANDOM RELATIVE ERROR CONTRIBUTION. TOT IS THE TOTAL RELATIVE ERROR. "OBSERV." IS FOR THE TERMS OF (9), "TIME AVG." IS FOR THE TERMS OF (11), AND "SPACE AVG." IS FOR THE TERMS OF (14)

METEOSAT-7 0°E							
	$\delta_r\widetilde{L}_a$	$\delta_r\widetilde{L}_s$	$\delta_r\widetilde{L}_m$	$\delta_r\widetilde{L}_\xi$	δK_T	RAND.	TOT.
	DESERT						
OBSERV. $\delta_r c_f$	1.8	12.4	4.1	3.8	0.9		13.9
TIME AVG. $\delta_r \bar{c}_f$	1.9	12.5	4.2	3.8		0.4	13.9
SPACE AVG. $\delta_r \widehat{\bar{c}}_f$			4.1	3.8		1.6	5.9
	SEA						
OBSERV. $\delta_r c_f$	8.6		3.1	7.7	2.8		12.0
TIME AVG. $\delta_r \bar{c}_f$	8.7		3.2	7.7		2.3	12.4
SPACE AVG. $\delta_r \widehat{\bar{c}}_f$			3.2	7.7		3.0	8.9

TABLE II
AS TABLE I BUT FOR METEOSAT-5 LOCATED AT 0°

METEOSAT-5 0°							
	$\delta_r\widetilde{L}_a$	$\delta_r\widetilde{L}_s$	$\delta_r\widetilde{L}_m$	$\delta_r\widetilde{L}_\xi$	δK_T	RAND.	TOT.
	DESERT						
OBSERV. $\delta_r c_f$	1.8	12.4	4.1	14.2	1.1		19.5
TIME AVG. $\delta_r \bar{c}_f$	1.9	12.5	4.2	14.2		0.3	19.5
SPACE AVG. $\delta_r \widehat{\bar{c}}_f$			4.2	14.2		1.1	14.9
	SEA						
OBSERV. $\delta_r c_f$	8.9		3.1	17.0	4.0		19.5
TIME AVG. $\delta_r \bar{c}_f$	8.8		3.1	17.1		1.9	19.6
SPACE AVG. $\delta_r \widehat{\bar{c}}_f$			3.1	17.1		2.9	17.8

TABLE III
AS TABLE I BUT FOR METEOSAT-5 LOCATED AT 63°E

METEOSAT-5 63°E							
	$\delta_r\widetilde{L}_a$	$\delta_r\widetilde{L}_s$	$\delta_r\widetilde{L}_m$	$\delta_r\widetilde{L}_\xi$	δK_T	RAND.	TOT.
	DESERT						
OBSERV. $\delta_r c_f$	1.9	12.9	3.9	14.1	1.1		19.8
TIME AVG. $\delta_r \bar{c}_f$	1.8	12.8	3.9	14.1		0.5	19.7
SPACE AVG. $\delta_r \widehat{\bar{c}}_f$			3.9	14.1		1.6	14.8
	SEA						
OBSERV. $\delta_r c_f$	22.4		3.4	17.1	4.2		28.4
TIME AVG. $\delta_r \bar{c}_f$	20.9		3.3	17.1		2.2	27.7
SPACE AVG. $\delta_r \widehat{\bar{c}}_f$			3.4	17.1		3.6	17.9

spaceborne instruments. To this end, observations acquired over the desert targets by the ATSR-2 instrument flying on the European Remote Sensing Satellite-2 (ERS-2), the SeaWiFS instrument onboard the National Aeronautics and Space Administration (NASA) SeaStar spacecraft, the VEGETATION radiometer on the French "Système pour l'Observation de la Terre" (SPOT-4) platform, and finally MERIS flying on the European Space Agency Environmental Research Satellite (ENVISAT) have been simulated accounting for the actual observation conditions and spectral responses [16]. The relative bias between these observations and the calibration reference weighted by the MVIRI VIS band is $+1.1\%$ with respect to ATSR-2, i.e., Meteosat calibration reference overestimates by $+1.1\%$ ATSR-2 radiances, -2.1% with respect to SeaWiFS, $+4.2\%$ with respect to VEGETATION and $+2.1\%$ with respect to MERIS. The corresponding mean weighted bias is close to $+1.5\%$. Thus, Meteosat calibration reference seems to underestimate by about 1% to 2% radiances observed by well-calibrated instrument, which is much smaller than the radiative transfer model intrinsic error δR_m of about 4% (Table I). These comparisons demonstrate that: 1) our calibration reference is reliable; 2) our error estimation of δR_m is rather conservative; and 3) the remaining random contribution of the calibration error, about 1.5%, is realistic.

Second, an independent estimation of $\breve{c}_f$ and $\mathcal{D}_f$ has been performed based on a cross calibration with the CERES instruments. This cross-calibration method, described in Appendix D, has been applied to the periods listed in Table V. Results, shown in Fig. 9 and Table IV for Meteosat-7, reveal the very good agreement between the calibration coefficients derived with our method and those derived from the cross calibration, both in terms of magnitude and estimated error. The cross-calibration coefficient $\breve{c}^*_f(t_0)$ estimated at launch date, 0.944 $\text{Wm}^{-2}\text{sr}^{-1}$/DC, exceeds $\breve{c}_f(t_0)$ by only 3%. This *a posteriori* error estimation, i.e., the difference between $\breve{c}_f(t_0)$ and $\breve{c}^*_f(t_0)$, compares favorably with the *a priori* error estimation $\delta_r\breve{c}_f(t_0)$, which is equal to 2.5%. Once again, according to this comparison, our calibration coefficient seems to be slightly underestimated, as is the case for the RTM evaluation [16]. For the evaluation of the Meteosat-5 calibration, 15 days of CERES-TRMM data were acquired in July and August 1998. During that period, the CERES-derived calibration coefficient is 0.902 $\text{Wm}^{-2}\text{sr}^{-1}$/DC, whereas the coefficient derived from the daily drift (17) is 0.894 $\text{Wm}^{-2}\text{sr}^{-1}$/DC. These results agree within 1%. The yearly Meteosat-5 sensor drift, about 1.3%, has not been evaluated against CERES but compares favorably with the value derived by [22]. This author found a yearly drift of 1.1% for the period 1994–1997, but without the correction of the NSR proposed in [14].

Third, our results have been compared with airborne observations used for the calibration of the Meteosat-5 VIS band in July 1995, assuming a rectangular response in the 0.4–1.1-μm interval [5]. Such a method provides, thus, a calibration coefficient that depends on the TOA spectral shape of the observed target. During that field campaign, a coefficient equal to 1.10 $\text{Wm}^{-2}\text{sr}^{-1}$/DC has been derived over a Tunisian desert site. During the same period, a mean coefficient of 1.13 $\text{Wm}^{-2}\text{sr}^{-1}$/DC has been derived with our algorithm simulating a similar calibration mechanism, which overestimates by only 3% the coefficient derived from airborne measurements [12].

Finally, the consistency between the Meteosat-5 and -7 VIS band TOA radiances has been controlled to evaluate the benefit of the Meteosat-5 NSR postlaunch adjustment [14]. TOA radiances have been acquired under similar viewing and sun zenith angles, i.e., when the relative azimuth angles are close to zero or 180°. Such situations occur at local noon along a longitudinal profile located at 31.5°E. There is good agreement between both instruments as can be seen in Fig. 10, left plot. A

TABLE IV
VIS BAND CALIBRATION COEFFICIENT (WATTS PER SQUARE METER PER STERADIAN PER DIGITAL COUNT) ESTIMATED AT THE LAUNCH DATE AND DAILY DRIFT IN FOR METEOSAT-5 AND -7 (WATTS PER SQUARE METER PER STERADIAN PER DC PER DAY). $\tilde{I}$ IS THE SOLAR IRRADIANCE WITHIN THE VIS BAND. $\tilde{\xi}$ IS THE INTEGRAL OF THE NSR. (∗) CALIBRATION DERIVED FROM THE CERES CROSS CALIBRATION

Met	$\breve{c}_f(t_0)$ $Wm^{-2}sr^{-1}$/DC	$\delta\breve{c}_f(t_0)$ %	$\mathcal{D}_f$ $Wm^{-2}sr^{-1}$/DC/day	$\delta\mathcal{D}_f$ %	$\tilde{I}$ Wm^{-2}	$\tilde{\xi}$ μm
5	0.818	±0.0749	2.818^{-5}	$\pm 2.392^{-5}$	691	0.504
7	0.916	±0.0233	5.523^{-5}	$\pm 1.953^{-5}$	691	0.504
7*	0.944	±0.0230	5.778^{-5}	$\pm 1.476^{-5}$	–	–

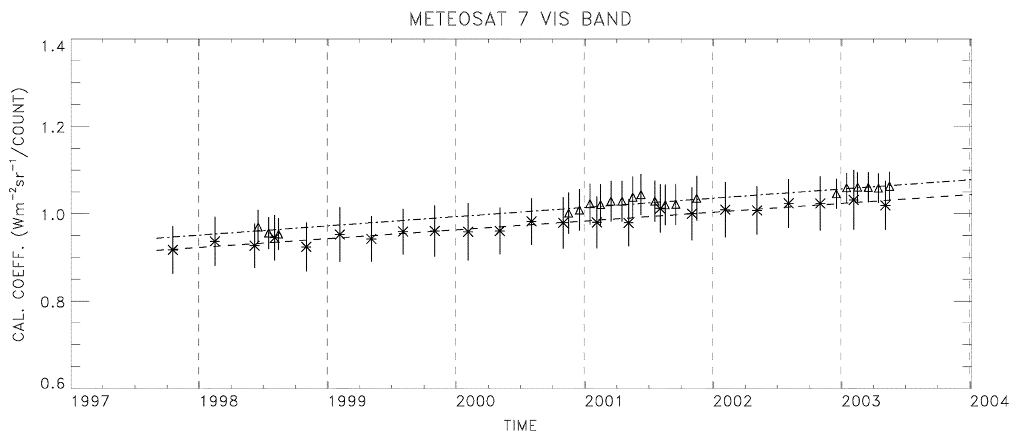

Fig. 9. (Dashed–dotted line) Meteosat-7 sensor drift derived the CERES-based calibration (△ symbol). (Dotted line) Sensor drift derived with our method (∗ symbol).

TABLE V
CERES DATA USED FOR VALIDATION: DATES, NUMBER OF DAYS IN RAP MODE DURING THE PERIOD, CERES INSTRUMENT (PFM = PROTO FLIGHT MODEL, FM = FLIGHT MODEL) AND SPACECRAFT

Period	Nbr of days	Instrument	Platform
4 June 1998 to 24 Aug. 1998	22	PFM	TRMM
1 Nov. 2000 to 26 Nov. 2001	296	FM1 and FM2	Terra
1 Dec. 2002 to 31 May 2003	175	FM2	Terra

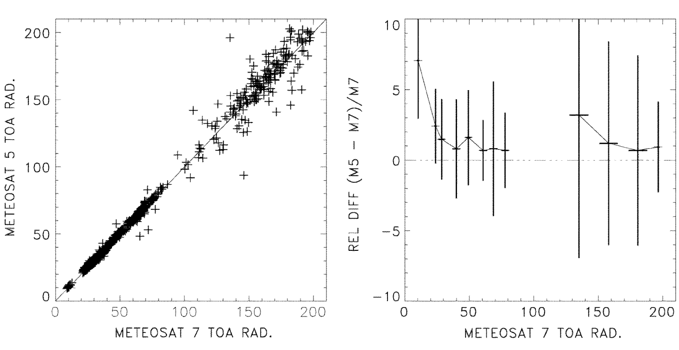

Fig. 10. (Left) TOA radiance (watts per square meter per steradian) scatter plot derived from Meteosat-7 and -5 along the 31.5°E latitudinal transect in 1999. (Right) Relative difference in percent between the Meteosat-7 and -5 TOA radiance as a function of the Meteosat-7 TOA radiance.

detailed analysis of the relative difference between both signals, shown in the right panel, reveals however some discrepancy, in particular over dark sea surfaces, where TOA radiance is close to 10 $Wm^{-2}sr^{-1}$ in the Meteosat VIS band. Such result might indicates some minor linearity problem with one of the instrument. The sharp transition between sea and terrestrial surfaces, where the TOA radiance typically ranges 20 and 90 $Wm^{-2}sr^{-1}$ in the present case, rather advocates a possible Meteosat-5 spectral response error around 0.4 μm, where spectral radiance over sea takes its maximum value. Over terrestrial surfaces and cloudy pixels, observed radiances agree within 1% to 2% on the average. This comparison also demonstrates that both instruments respond linearly to intensity within the limit of the digitalization, as a 5% difference over sea surfaces corresponds to about half a digital count value.

VI. CONCLUSION

This paper presents a new method developed for the routine calibration of the MVIRI VIS band onboard the Meteosat satellites. The proposed vicarious approach relies on calculated radiances over targets with different spectral properties, i.e., sea and bright deserts. The method includes an advanced *a priori* estimation of the calibration error accounting for both the radiometric and simulation uncertainties. As the NSR characterization errors have not been established prior to the launch, a simple conceptual model is proposed to assess this error. So far, this model does not account for NSR aging, i.e., this error contribution is constant in time. Difference in the sensor drift derived over desert and sea targets suggests, however, that the magnitude of sensor sensitivity degradation might not be constant over the VIS band spectral interval.

The estimated calibration error for each application cycle of the algorithm is about 6% for Meteosat-7, which has the most accurately characterized NSR. Meteosat-5 calibration results clearly reveals the impact of any NSR uncertainty on the calibration error, 15% in this case. However, a comparison of

TOA radiances acquired by the Meteosat-5 and -7 instruments indicates that this impact has probably been overestimated, as the difference between the TOA radiance does not exceed 5%. RTM accuracy evaluation and an independent calibration method based on CERES observations demonstrated that our calibration error estimation is realistic. This comparison provides also a similar Meteosat-7 sensor drift value. Most of the validation results presented here seem to indicate that the calibration coefficient derived for Meteosat-7 might be underestimated by about 2%. Such an error is, however, largely within the error due to the NSR uncertainty. This operational calibration algorithm allows thus the derivation of a consistent estimation of the error and to place a control on the reliability on the instrument actual characteristics. This new calibration method can be applied to the entire Meteosat archive, increasing thereby the value of this archive in support to climate monitoring.

APPENDIX
A. MVIRI VIS BAND

Meteosat image line (row) and pixel (column) acquisition results from a combination of the main mirror rotation and satellite spin. A complete description of the MVIRI instrument can be found on the EUMETSAT web page http://www.eumetsat.de. The VIS band of MVIRI is composed of two detectors scanning simultaneously two lines of pixels plus two backup detectors in case of failure of the two operational ones. An offset voltage of about 100 mV is added to the the detector electronics and is responsible for a mean offset value of about five counts when the instrument is pointing to space. Note that this offset voltage has been implemented for the first time onboard Meteosat-4. The total spectral response of a VIS band detector is essentially determined by the reflectance and transmittance properties of the telescope optics and the silicon photodiode detector as there is no spectral filter. These properties have not been very accurately measured in the past. A simple model is, thus, proposed to characterize the spectral response uncertainty. At a particular wavelength λ, it is assumed that the NSR characterization error is due to: 1) an uncertainty $\epsilon_\lambda(\lambda)$ in the absolute wavelength determination, i.e., the imprecision Δ_λ of the exact wavelength at which the measurement took place; 2) measurement error of the optic and detector transmittance $\epsilon_t(\lambda)$, and finally 3) extrapolation errors $\epsilon_e(\lambda)$ outside the 0.5–0.9-μm interval

$$\delta\xi(\lambda) = \sqrt{\epsilon_\lambda^2(\lambda) + \epsilon_t^2(\lambda) + \epsilon_e^2(\lambda)} \tag{19}$$

with $\epsilon_\lambda(\lambda) = (\partial\xi(\lambda)/\partial\lambda)\Delta_\lambda$. As no prelaunch measurements of the transmittance uncertainty are available, $\epsilon_t(\lambda)$ is estimated from the difference between the response of the four detectors for each wavelength. The error due to extrapolation outside the 0.5–0.9-μm interval at wavelength λ_e is estimated with

$$\epsilon_e(\lambda) = \epsilon_e \frac{|\lambda_e - \lambda_b|}{|\lambda_b - \lambda_l|} \tag{20}$$

where ϵ_e is the assigned maximum error due to the extrapolation. λ_b and λ_l are equal to 0.5 and 0.35 μm or 0.9 and 1.28 μm, respectively. Estimated errors are shown in Fig. 1 for Meteosat-7 and on Fig. 11 for the other Meteosat instruments.

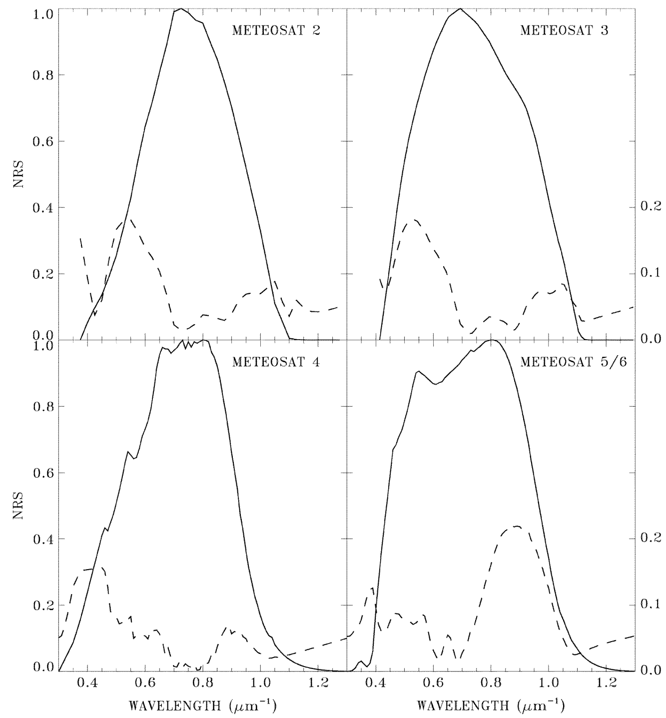

Fig. 11. (Solid line) NSR of the MVIRI VIS band onboard the Meteosat–2 to –6 satellites. (Dashed lines) Estimated NSR error.

Calibration relies on the use of rectified and equalized images (level 1.5) for which it is not possible anymore to determine which of the two VIS band detectors has been used for the acquisition of a specific pixel. The estimation of the radiometric noise used in (5) accounts, thus, for the detector noise and the difference between the offset of each detector

$$\delta K_{1.5} = \sqrt{\frac{1}{8}\sum_d \left(\sigma_{\hat{K}_0}(d)\right)^2 + \left(\frac{\hat{K}_0(d_1) - \hat{K}_0(d_2)}{N_l}\right)^2} \tag{21}$$

where $\sigma_{\hat{K}_0}(d)$ is the detector offset standard deviation of one image corner, i.e., when the instrument is pointing to deep space, and the factor 8 corresponds to the two VIS band detectors times the four space corners. $\hat{K}_0(d_1)$ and $\hat{K}_0(d_2)$ are the mathematical mean offset value of VIS detector 1 and 2, respectively. N_l is the number of lines covering a calibration target.

B. CALIBRATION TARGET CHARACTERIZATION

A. Bright Desert

A series of 19 radiometrically stable and bright targets, located in the Saharan and Saudi Arabian deserts (see Fig. 2), have already been identified by [18] and their stability confirmed by [23]. These arid targets are large uniform areas, essentially consisting of sand dunes, gravel, and rocks. The surface bidirectional reflectance of these sites is represented with a simple bare soil model [17], coupled with the 6S radiative transfer code, which has been modified to account for directional effects in case of nonconstant surface spectral conditions within the spectral interval of integration. This bare soil BRF model depends on three state variables, namely, the single-scattering albedo, the asymmetry of the phase function, and finally a porosity parameter. The value of these parameters over each site has been derived from Polarization and Directionality of Earth's Reflectances (POLDER) observations [24]. Regarding the atmospheric properties, the principal state variables controlling TOA radiances over bright surfaces in the 0.4–1.6-μm spectral range are the total column water vapor, the total column ozone, and the aerosol optical thickness. A US62 vertical atmospherical profile and desert dust aerosol type [25] are assumed all year long. An aerosol optical thickness climate dataset has been derived from Total Ozone Mapping Spectrometer (TOMS) absorbing aerosol index (AI) and Aerosol Robotic Network (AERONET) bservations. The elaboration of the surface and atmospheric datasets are described in [16].

B. Sea Surface

The aerosol optical thickness and surface wind speed are the main two state variables that govern TOA radiance over sea surfaces in the MVIRI VIS band. The ocean color, total column water vapor, and ozone contribute also to the observed radiances, but only to a lesser extent. Hence, clear ocean areas used for the calibration have been chosen far from any continents, where the tropospherical aerosol and ocean pigment concentrations are expected to be minimum (Fig. 2). Simulations are performed with the 6S code, assuming a US62 vertical profile and oceanic aerosol type all year long. A climate dataset of aerosol properties corresponding to very clear days are derived from AERONET observations. Typical values range between 0.03–0.07. The surface wind speed and total column water vapor are taken from ECMWF analyzed data. A monthly mean ozone climate dataset has been built from several years of TOMS observations, with a typical standard deviation of about 15%. Currently, the ocean color is determined for a fixed pigment concentration of 0.2 mg $\cdot$ m^{-3}.

C. Daily Cycle Analysis

The consistency between observation and simulation is verified according to a method proposed in [21]. Let $\hat{K}(t_1, g)$ and $\hat{K}(t_2, g)$ be two observations over target g acquired at time t_1 and t_1, i.e., with different SZAs. The different SZAs of these two observations will be responsible for a change in the count values resulting from different illumination conditions and surface and atmospheric scattering and absorption processes. When this change is large enough, i.e., bigger than the radiometric error, and the offset value K_0 constant during the day, a calibration coefficient can be derived from this pair

$$c'_f(t_{1,2}, g) = \frac{\tilde{R}_f(t_2, g) - \tilde{R}_f(t_1, g)}{\hat{K}(t_2, g) - \hat{K}(t_1, g)}. \tag{22}$$

As can be seen, the computation of this calibration does not require the knowledge of the offset K_0. The zero intercept (offset) value could now be estimated independently from the radiometer deep space observations from (22)

$$K'_0(t_{1,2}) = \hat{K}(t_1, g) - \frac{\tilde{R}_f(t_1, g)}{c'_f(t_{1,2}, g)}. \tag{23}$$

The nonlinear change in magnitude from $\tilde{R}_f(t_1, g)$ to $\tilde{R}_f(t_2, g)$ due to changing angular configurations should be linearly related to the difference between $\hat{K}(t_1, g)$ and $\hat{K}(t_2, g)$ so that $K'_0(t_{1,2}) \rightarrow K_0(t)$ when the simulations are reliable. A linear regression $R(k) = a_0 + b_0 K$ is computed assuming errors in both R and K coordinates. The error on the estimation of a_0 and b_0 at confidence α is derived with

$$\delta a_0 = t_{\alpha/2}(N_g - 1)\frac{\sigma_{a_0}}{\sqrt{N_g}} \tag{24}$$

$$\delta b_0 = t_{\alpha/2}(N_g - 1)\frac{\sigma_{b_0}}{\sqrt{N_g}} \tag{25}$$

where σ_{a_0} and σ_{b_0} are the standard deviation of a_0 and b_0, respectively. $\bar{c}'_f(b, g)$ and $\bar{K}'_0(g)$ are derived from a_0 and b_0 with $\bar{c}'_f(b, g) = b_0$ and $\bar{K}'_0(g) = -a_0/b_0$. The corresponding errors are

$$\delta\bar{c}'_f(g) = \delta b_0 \tag{26}$$

$$\delta\bar{K}'_0(b) = \sqrt{\left(\frac{a_0 \delta b_0}{b_0^2}\right)^2 + \left(\frac{\delta a_0}{b_0}\right)^2}. \tag{27}$$

The coefficient $\bar{c}_f(g)$ derived for target g is assumed not reliable when

$$|\bar{c}'_f(g) - \bar{c}_f(g)| > \sqrt{(\delta\bar{c}'_f(g))^2 + (\delta\bar{c}_f(g))^2} \tag{28}$$

$$|\bar{K}'_0(g) - \hat{\bar{K}}_0| > \sqrt{(\delta\bar{K}'_0(g))^2 + (\delta\hat{\bar{K}}_0)^2} \tag{29}$$

where $\bar{K}'_0$ is the mean offset value during the period $[p_1, p_2]$.

D. CERES Cross-Calibration Method

The CERES instruments acquire radiance observations in the 0.3–5.0-μm interval with an estimated calibration accuracy better than 1% [26]. As the CERES radiometer provides broadband measurements, relationships between the Meteosat effective radiance $\tilde{L}$ in the VIS band and broadband radiance L_{BB} have been derived with a third-order regression

$$\tilde{L}_{\mathrm{BB}} = c_0 + c_1\tilde{L} + c_2\tilde{L}^2 + c_3\tilde{L}^3. \tag{30}$$

A best estimate of the coefficients c_i of (30) has been established using a database of simulated TOA spectral radiances [27]. The radiative transfer computations were performed with the Santa Barbara DISORT atmospheric radiative transfer (SBDART) model [28] for 4622 surface and atmospheric conditions and for nine values for the solar zenith angle ranging from 0° up to 80°. Cloudy and cloud-free atmospheric conditions are equally represented in these scenarios. According to the predominant properties of the surface, these spectral curves were classified as "ocean" or "land," whatever the cloud cover. A distinct set of regression coefficients c_i of (30) has been derived for these two classes and for the nine solar zenith angles. For each of these regressions, the root mean square of the error introduced by the effective to broadband radiance conversion is about 4% with a bias of about 2.6%.

CERES data corresponding to the rotating azimuth plane (RAP) operating mode [26] of the instrument were preferably selected to ensure a uniform spatial distribution of the coangular Meteosat and CERES observations. Periods of acquisition are reported in Table V. A series of colocated and coangular CERES and Meteosat observations were collected during each CERES observation period, with a maximum phase angle of 20° between CERES and Meteosat. For each observation pair, the Meteosat pixels corresponding to the CERES footprint center were extracted provided that the pixel value relative range within the CERES footprint did not exceed 30%. The cross-calibration coefficient c_f^* is derived by substituting (3) in (30)

$$\tilde{L}_{\mathrm{BB}} = c_0 + c_1 c_f^*(K - K_0) + c_2(c_f^*(K - K_0))^2 + c_3(c_f^*(K - K_0))^3 \quad (31)$$

where the coefficients c_i are selected according to the sun zenith angle and the surface type using the International Geosphere-Biosphere Program (IGBP) class cover map [29]. For comparison purposes with the $\hat{\bar{c}}_f$ values, coefficients c_f^* have been averaged over monthly periods. The estimation of the corresponding error $\delta \bar{c}_f^*$ assumes that the CERES calibration accuracy ($\epsilon_C = 0.01$) is responsible for a systematic error. Errors due to the effective to broadband radiance conversion are decomposed into a systematic contribution which includes the MVIRI VIS band NSR uncertainty and a random contribution that accounts for all errors related to the differences in illumination and viewing angles as well as target nonhomogeneity. Hence, the error $\delta \bar{c}_f^*$ of the mean coefficient $\bar{c}_f^*$ writes

$$\delta \bar{c}_f^* = \sqrt{(\epsilon_C \bar{c}_f^*)^2 + (\delta_{r\,\mathrm{BB}} \bar{c}_f^*)^2 + \frac{t_{\alpha/2}^2(N_C - 1)}{N_C} \sigma_{\bar{c}_f^*}^2} \quad (32)$$

where $\delta_{r\,\mathrm{BB}}$ is the mean bias during the monthly period due to the broadband conversion, N_C is the number of Meteosat–CERES pairs during the same period and $\sigma_{\bar{c}_f^*}$ the standard deviation of $\bar{c}_f^*$. $\delta_{r\,\mathrm{BB}}$ is estimated as the maximum range of c_f^* values derived over spectrally different scenes. Coefficients $\bar{c}_f^*$ are used to determine the calibration coefficient at launch time $\breve{c}_f^*(t_0)$ and the daily drift $\mathcal{D}^*$ as explained in Section III-E.

ACKNOWLEDGMENT

The authors are grateful to A. Nock, T. Heinemann, and A. Lattanzio for their dedicated support in handling Meteosat data and to A. Arriaga and J. Müller for their fruitful comments and suggestions. Additional information on the Meteosat radiometer VIS band calibration is available at the EUMETSAT web page http://www.eumetsat.de.

REFERENCES

[1] M. Y. Govaerts, "Exploitation of the Meteosat archive for climate monitoring: Expectations and limitations," in *Proc. 1999 EUMETSAT Meteorological Satellite Data User's Conf.* Copenhagen, Denmark, 1999, pp. 255–262.

[2] J. F. L. Marshall, J. J. Simpson, and Z. Jin, "Satellite calibration using a collocated nadir observation technique: Theoretical basis and application to the GMS-5 pathfinder benchmark period," *IEEE Trans. Geosci. Remote Sensing*, vol. 37, pp. 499–507, Jan. 1999.

[3] F. Cabot, G. Dedieu, and P. Maisongrande, "Monitoring NOAA/AVHRR and Meteosat shortwave bands calibration and inter calibration over stable areas," in *Physical Measurements and Signatures in Remote Sensing, Proc. 6th ISPRS Symp.*, Val d'Isere, France, 1994, pp. 41–46.

[4] W. B. Rossow, C. L. Brest, and M. D. Roitier, "International Satellite Cloud Climatology Project (ISCCP): New radiance calibrations," WMO, Geneva, Switzerland, Tech. Rep. WMO/TD-No 736, 1996.

[5] K. T. Kriebel and V. Amann, "Vicarious calibration of the meteosat visible channel," *J. Atmos. Oceanograph. Technol.*, vol. 10, pp. 225–232, 1993.

[6] P. Koepke, "Vicarious satellite calibration in the solar spectral range by means of calculated radiances and its application to Meteosat," *Appl. Opt.*, vol. 21, pp. 2845–2854, 1982.

[7] C. Moulin, C. E. Lambert, J. Poitou, and F. Dulac, "Long term (1983–1994) calibration of the Meteosat solar (VIS) channel using desert and ocean targets," *Int. J. Remote Sens.*, vol. 17, pp. 1183–1200, 1996.

[8] A. Arriaga and J. Schmetz, "Calibration of the Meteosat-5/-6 VIS channels with help of modeled radiances," *Contribut. Atmos. Phys.*, vol. 72, pp. 133–139, 1999.

[9] J. Schmetz, "Operational calibration of the Meteosat water vapor channel by calculated radiances," *Appl. Opt.*, vol. 28, pp. 3030–3038, 1989.

[10] M. Gube, V. Gaertner, and J. Schmetz, "Analysis of the operational calibration of the Meteosat infrared-window channel," *Meteorol. Appl.*, vol. 3, pp. 307–316, 1996.

[11] C. Moulin, F. Guillard, F. Dulac, and C. E. Lambert, "Long-term daily monitoring of Saharan dust load over ocean using Meteosat ISCCP-B2 data. 1. Methodology and preliminary results for 1983–1994 in the mediterranean," *J. Geophys. Res.*, vol. 102, pp. 16 947–16 958, 1997.

[12] K. T. Kriebel, H. Mannstein, and V. Amann, "Absolute calibration of the Meteosat-5 visible channels," in *Proc. 1996 Meteorological Satellite Data Users' Conf.* Vienna, Austria, 1996, pp. 31–40.

[13] A. P. Trishchenko, G. Fedosejevs, Z. Li, and J. Cihlar, "Trends and uncertainties in thermal calibration of AVHRR radiometers onboard NOAA-9 to NOAA-16," *J. Geophys. Res.*, vol. 107, 2002. DOI:10.1029/2002JD002353.

[14] Y. M. Govaerts, "Correction of the Meteosat-5 and -6 VIS band relative spectral response with Meteosat-7 characteristics," *Int. J. Remote Sens.*, vol. 20, pp. 3677–3682, 1999.

[15] Y. M. Govaerts, A. Arriaga, and J. Schmetz, "Operational vicarious calibration of the MSG/SEVIRI solar channels," *Adv. Space Res.*, vol. 28, pp. 21–30, 2001.

[16] Y. M. Govaerts and M. Clerici, "Evaluation of radiative transfer simulations over bright desert calibration sites," *IEEE Trans. Geosci. Remote Sensing*, vol. 42, pp. 176–187, Jan. 2004.

[17] B. Pinty, M. M. Verstraete, and R. Dickinson, "A physical model for predicting bidirectional reflectances over bare soil," *Remote Sens. Environ.*, vol. 27, pp. 273–288, 1989.

[18] H. Cosnefroy, M. Leroy, and X. Briottet, "Selection and characterization of Saharan and Arabian desert sites for the calibration of optical satellite sensors," *Remote Sens. Environ.*, vol. 58, pp. 101–114, 1996.

[19] E. F. Vermote, D. Tanré, J. L. Deuzé, M. Herman, and J. J. Morcrette, "Second simulation of the satellite signal in the solar spectrum, 6S: An overview," *IEEE Trans. Geosci. Remote Sensing*, vol. 35, pp. 675–686, May 1997.

[20] A. Lyapustin, "Radiative transfer code SHARM-3D for radiance simulations over a non-Lambertian nonhomogeneous surface: Intercomparison study," *Appl. Opt.*, vol. 41, pp. 5607–5615, 2002.

[21] Y. M. Govaerts, B. Pinty, M. M. Verstraete, and J. Schmetz, "Exploitation of angular signatures to calibrate geostationary satellite solar channels," in *Proc. IGARSS* Seattle, WA, 1998, pp. 327–329.

[22] C. Moulin and X. Schneider, "Calibration of the Meteosat-5 sensor visible channel," *Int. J. Remote Sens.*, vol. 20, pp. 195–200, 1999.

[23] M. Capderou, "Study of the stability of the ScaRaB shortwave channel. Application: Determination of uniform desert zone," *Int. J. Remote Sens.*, vol. 19, pp. 3641–3669, 1998.

[24] P. Bicheron and M. Leroy, "BRDF signatures of major biomes observed from space," *J. Geophys. Res.*, vol. 105, pp. 26 669–26 682, 2000.

[25] E. P. Shettle and R. W. Fenn, "Models for the aerosols of the lower atmosphere and the effects of humidity variations on their optical properties," U.S. Air Force Geophysics Lab., Hanscomb AFB, MA, Tech. Rep. AFGL-TR-79-0214, 1979.

[26] B. A. Wielicki, B. R. Barkstrom, E. F. Harrison, R. B. L. III, G. L. Smith, and J. E. Cooper, "Clouds and the Earth's Radiant Energy System (CERES): An earth observing system experiment," *Bull. Amer. Meteorol. Soc.*, vol. 77, pp. 853–868, 1996.

[27] N. Clerbaux, S. Dewitte, L. Gonzalez, C. Bertand, B. Nicula, and A. Ipe, "Outgoing longwave flux estimation: Improvement of angular modeling using spectral information," *Remote Sens. Environ.*, vol. 85, pp. 389–395, 2003.

[28] P. Ricchiazzi, S. Yang, C. Gautier, and D. Sowle, "SBDART: A research and teaching software tool for plane-parallel radiative transfer in the earth's atmosphere," *Bull. Amer. Meteorol. Soc.*, vol. 79, pp. 2101–2114, 1998.

[29] J. R. G. Townshend, C. O. Justice, D. Skole, J.-P. Malingreau, J. Cihlar, P. Teillet, F. Sadowski, and S. Ruttenberg, "The 1 km resolution global data set: Needs of the international geosphere biosphere programme," *Int. J. Remote Sens.*, vol. 15, pp. 3417–3441, 1994.

Yves M. Govaerts received the Ph.D. degree in physics from the Université Catholique de Louvain, Louvain-la-Neuve, Belgium, in 1995.

He was a Research Scientist with the Royal Meteorological Institute of Belgium, Brussels, from 1990 to 1992. From 1993 to 1997, he was with the Space Applications Institute, Ispra, Italy. In 1997, he had a Postdoctoral Fellowship from the European Space Agency, Noordwijk, The Netherlands, to work on the design of vegetation indexes for the MERIS instrument. Since 1997, he has been with EUMETSAT, Darmstadt, Germany. His principal research fields are radiative transfer modeling, the development of operational retrieval algorithms for the characterization of land surface properties, and the development of vicarious calibration methods applied to the European geostationary meteorological satellites.

Marco Clerici received the B.S. degree (with honors) in electronic engineering, specializing in microelectronics and instrumentation, from the University Politecnico di Milano, Milan, Italy, in 1993.

From 2000 to 2004, he developed at EUMETSAT the MSG/SEVIRI vicarious calibration algorithm and provided support for the development of radiative transfer models. Since 2004, he has been with the Joint Research Centre of the European Commission, Ispra, Italy, where his activity focuses on ocean color retrieval from polar orbiting satellite data. His main interest is in the area of scientific algorithm development and validation, radiative transfer modeling, statistical data analysis, remote sensing, and satellite data processing.

Nicolas Clerbaux received an engineering degree in applied physics from the Université Libre de Bruxelles, Brussels, Belgium, in 1992.

He is currently an Assistant Research Scientist in the Remote Sensing from the Space Section, Royal Meteorological Institute of Belgium, Brussels. His research interests focus on the inversion of satellite measurements for the evaluation of the earth radiation budget.